Interplay between localized and itinerant magnetism in Co-substituted $FeGa_3$

A. A. Gippius,[1,2,*] V. Yu. Verchenko,[3,4] A. V. Tkachev,[1,2] N. E. Gervits,[2] C. S. Lue,[5] A. A. Tsirlin,[4] N. Büttgen,[6] W. Krätschmer,[6] M. Baenitz,[7] M. Shatruk,[8] and A. V. Shevelkov[3]

[1]*Department of Physics, Moscow State University, 119991, Moscow, Russia*
[2]*A.V. Shubnikov Institute of Crystallography, 119333, Moscow, Russia*
[3]*Department of Chemistry, Moscow State University, 119991, Moscow, Russia*
[4]*National Institute of Chemical Physics and Biophysics, Tallinn, Estonia*
[5]*Department of Physics, National Cheng Kung University, 70101, Tainan, Taiwan*
[6]*Experimental Physics V, University of Augsburg, 86159, Augsburg, Germany*
[7]*Max Planck Institute for Chemical Physics of Solids, 01187 Dresden, Germany*
[8]*Department of Chemistry and Biochemistry, Florida State University, Tallahasee, Florida 32306, USA*

(Received 31 October 2013; revised manuscript received 17 March 2014; published 31 March 2014)

The evolution of the electronic structure and magnetic properties with Co substitution for Fe in the solid solution $Fe_{1-x}Co_xGa_3$ was studied by means of *ab initio* band-structure calculations and nuclear spin-lattice relaxation $1/T_1$ of the ^{69,71}Ga nuclei. The $^{69,71}(1/T_1)$ was studied as a function of temperature in a wide temperature range of 2–300 K for the concentrations $x = 0.0$, 0.5, and 1.0. In the parent semiconducting compound $FeGa_3$, the temperature dependence of the $^{69}(1/T_1)$ exhibits a huge maximum at about $T \sim 6$ K indicating the existence of in-gap states. The opposite binary compound, $CoGa_3$, demonstrates a metallic Korringa behavior with $1/T_1 \propto T$. In $Fe_{0.5}Co_{0.5}Ga_3$, the relaxation is strongly enhanced due to spin fluctuations and follows $1/T_1 \propto T^{1/2}$, which is a unique feature of weakly and nearly antiferromagnetic metals. This itinerant antiferromagnetic behavior contrasts with *ab initio* band-structure calculations, where a ferromagnetic state with an ordered moment of 0.5 μ_B/f.u. is predicted. The results are discussed in terms of the interplay between the localized and itinerant magnetism including in-gap states and spin fluctuations.

DOI: 10.1103/PhysRevB.89.104426 PACS number(s): 71.20.Lp, 76.60.Es, 76.60.Gv

I. INTRODUCTION

Solid solutions based on $FeGa_3$ attracted much interest because of prospective thermoelectric applications and an intriguing low-temperature magnetic behavior. The parent binary compound $FeGa_3$ is a rare representative of nonmagnetic and semiconducting Fe-based intermetallic compounds [1] akin to the small-gap semiconductors FeSi [2,3] and $FeSb_2$ [4,5]. Because of the small value of the energy gap (E_g) and narrow energy bands, these compounds are considered as potential thermoelectric materials demonstrating extremely high Seebeck coefficient values of $|S| \approx 500$ mV/K at 50 K and $|S| \approx 45$ mV/K at 10 K for FeSi [6] and $FeSb_2$ [7], respectively. The value of E_g in $FeGa_3$ was determined by various theoretical and experimental techniques, including *ab initio* band-structure calculations ($E_g = 0.4$–0.5 eV) [8,9], high-temperature magnetometry ($E_g = 0.3$–0.5 eV) [10], photoelectron spectroscopy ($E_g \leqslant 0.8$ eV) [10], and resistivity measurements ($E_g = 0.14$ eV) [11]. As discussed in Ref. [9], the dominant contribution to the density of states (DOS) near the Fermi level in $FeGa_3$ comes from the Ga $4p$ states and from predominantly nonbonding Fe $3d$ states at the top of the valence band. The band gap originates from a strong hybridization of the Fe d and Ga p atomic orbitals. The formation of the energy gap in $FeGa_3$ is reminiscent of that in strongly correlated $3d$ and $4f$ Kondo insulators including FeSi and $FeSb_2$, which are likewise characterized by a small hybridization gap at the Fermi level [12,13].

It has been reported [14] that already a few percent cobalt doping in $FeGa_3$ drastically changes the properties of the parent compound. Namely, the 5% Co-doped $Fe_{0.95}Co_{0.05}Ga_3$ exhibits properties of a bad metal and a Curie-Weiss paramagnet, in contrast to semiconducting and nonmagnetic $FeGa_3$. Our *ab initio* band-structure calculations have shown that the Co doping shifts the Fermi level position towards the conduction band formed by the $3d$ (Fe/Co) and $4p$ (Ga) orbitals, thus leading to metallic properties and enabling precise tuning of the power factor $PF = S^2\sigma$ (Ref. [9]), where σ is the electrical conductivity. According to the resistivity data, the metallic state for the $Fe_{1-x}Co_xGa_3$ solid solution is achieved when $x = 0.125$ [9]. The end member of the solid solution, $CoGa_3$, exhibits good metallic properties with residual resistivity ratio at the order of 100 and a temperature-independent paramagnetic susceptibility of conduction electrons, which is, however, outweighed by the core diamagnetic contribution [1,14].

Remarkably, the Ge doping on the Ga site has an even more dramatic effect on the magnetism [15]. The $FeGa_{3-y}Ge_y$ solid solution reveals ferromagnetic ordering and an associated quantum critical behavior close to the critical concentration of $y_c = 0.13$, where the ferromagnetism emerges. In contrast, the $Fe_{1-x}Co_xGa_3$ solid solution remains paramagnetic or nearly paramagnetic for all Co concentration studied so far [15].

The $Fe_{1-x}Co_xGa_3$ solid solution exists for any Co concentration (x) and demonstrates a noticeable deviation from the Vegard behavior, even though the crystal structure and lattice symmetry remain the same for all Co concentrations [9]. This crystal structure should be considered as a three-dimensional framework constructed by polyhedra [Fig. 1(a)]. The main building unit is a pair of face-shared bicapped trigonal prisms

*Corresponding author: gippius@mail.ru

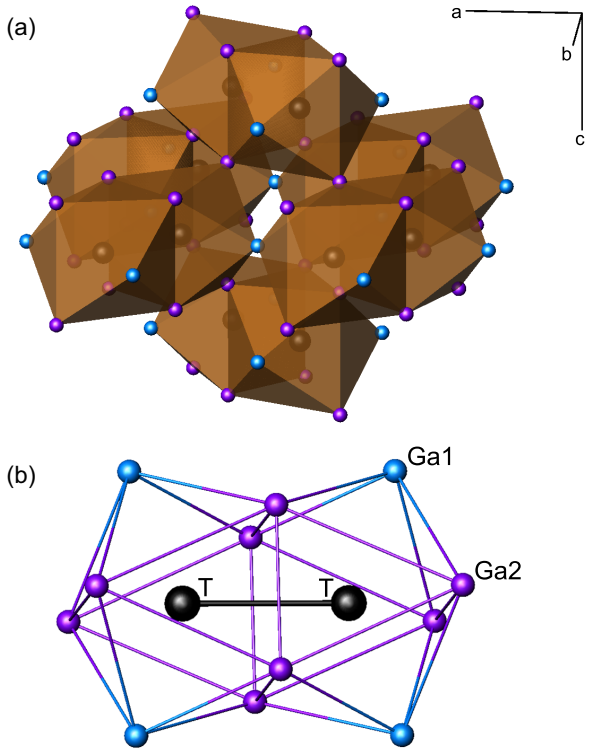

FIG. 1. (Color online) Polyhedral representation of the (a) crystal structure of the $Fe_{1-x}Co_xGa_3$ solid solution, and (b) its building unit—a pair of bicapped trigonal prisms centered by the T–T dumbbell.

centered by a T–T dumbbell, where T = Fe, Co [Fig. 1(b)]. The assembly of the building units is arranged in compliance with the four-fold screw axis, which is parallel to the c direction, such that face-shared filled prisms and empty spaces alternate in a staggered order. Thus the assembly of polyhedra constructs the entire, almost isotropic crystal structure. In support of this, the isostructural compounds $FeGa_3$ [16] and $RuIn_3$ [17] show no significant anisotropy in their transport properties. On the other hand, electronic properties and their evolution upon doping may critically depend on the local structure, i.e., whether the Fe–Fe, Fe–Co, or Co–Co dumbbells are formed [9]. While no ordering of the Fe and Co atoms was observed on the macroscopic level, the ^{69}Ga NQR local probe revealed the primary formation of homo-atomic pairs Fe–Fe and Co–Co, although the Fe–Co dumbbells are also present in a significant amount [9].

In this paper, we report the results of the systematic study of the evolution of the electronic structure and magnetic properties with Co substitution for Fe in the solid solution $Fe_{1-x}Co_xGa_3$, including *ab initio* band-structure calculations ($0 \leqslant x \leqslant 1$), ^{69,71}Ga and ^{59}Co NMR, and nuclear spin-lattice relaxation $1/T_1$ of the ^{69,71}Ga nuclei ($x = 0.0$, 0.5, and 1.0) in the temperature range 2–300 K.

II. EXPERIMENTAL

Single-phase powder samples of the $Fe_{1-x}Co_xGa_3$ solid solution for various x were prepared by mixing the elements (Fe: powder, Acros Organics 99%; Co: powder, Alfa Aesar 99.8%; Ga: bar, Aldrich 99.9999%) with the Fe:Co:Ga molar ratio of $(1-x) : x : 15$ using Ga both as a reactant and flux medium. Mixtures of the elements were sealed in precarbonized quartz ampoules under vacuum (less than 10^{-2} torr) and annealed in a programmable furnace at 900 °C for 55 hours to obtain a homogeneous melt. After this, a furnace was slowly cooled to 400 °C for 125 hours and further to ambient temperature for 5 hours. Excess Ga was separated at 40 °C using an Eppendorf 5804 R centrifuge, yielding needlelike silvery-gray crystals with a length up to several millimeters. The obtained crystals were purged from the remainder of Ga with diluted 0.5 M HCl and washed consecutively with distilled water and acetone. In our previous study of the solid solution $Fe_{1-x}Co_xGa_3$ [9], we found perfect agreement between the nominal and actual chemical composition of the obtained crystals using the EDX spectroscopy and established the composition dependence of the $Fe_{1-x}Co_xGa_3$ unit cell parameters. Thus, in the present study, we used x-ray powder diffraction technique (Bruker D8 Advance diffractometer, Cu-Kα_1 radiation, Lynxeye detector) to confirm both phase purity of the obtained crystals and their chemical composition using the calculated values of the cell parameters.

The ^{69,71}Ga NMR/NQR measurements were performed in the temperature range 2–300 K utilizing a home-built phase coherent pulsed NMR/NQR spectrometer. The ^{69,71}Ga NQR spectra were measured using a frequency step point-by-point spin-echo technique. At each frequency point, the area under the spin-echo magnitude was integrated in the time domain and averaged by a number of accumulations, which depends on the sample and temperature. Nuclear spin-lattice relaxation rates were measured using the so-called "saturation recovery" method. Nuclear magnetization recovery curves $M(t)$ were obtained from the recovery of the spin-echo magnitude as a function of the time interval τ between the saturation pulse comb and the $\frac{\pi}{2} - \pi$ spin-echo sequence.

III. RESULTS AND DISCUSSION

A. *Ab initio* calculations

The FPLO (full potential local orbitals) code was used for the electronic structure calculations [18]. FPLO performs density-functional (DFT) calculations within the local density approximation (LDA) for the exchange-correlation potential [19]. The integrations in the k space were performed by an improved tetrahedron method [20] on a grid of $12 \times 12 \times 12\,k$ points evenly spread in the first Brillouin zone. The calculation of the spin-polarized state of the $Fe_{1-x}Co_xGa_3$ solid solution was done in the following steps. Firstly, an optimization of atomic coordinates was performed for different x within the virtual crystal approximation (VCA) using the experimental values of lattice parameters [9]. Secondly, self-consistent spin-polarized calculations were performed for the relaxed structure. In addition to the VCA calculations, two types of ordering of the T atoms (T = Fe, Co) for $x = 0.5$ were investigated. Using the results of the crystal structure determination for $x = 0.5$ [9], we constructed two models, the first one with homonuclear Fe–Fe and Co–Co dumbbells (space group $Cmmm$, $a = b = 8.8298$ Å, $c = 6.4654$ Å) and the second one with heteronuclear Fe–Co dumbbells (space group

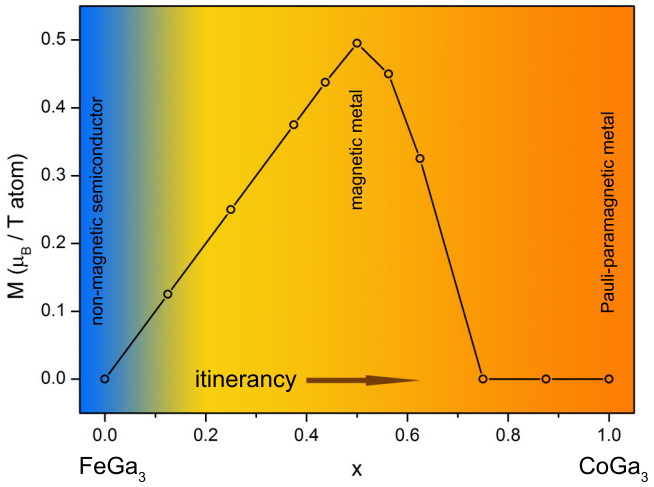

FIG. 2. (Color online) Total magnetic moment per T atom as a function of x in $Fe_{1-x}Co_xGa_3$ as obtained within the virtual crystal approximation.

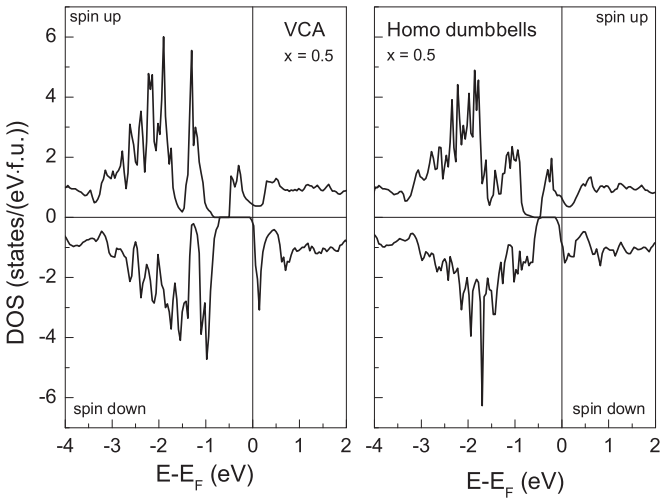

FIG. 3. Density of states plots for $x = 0.5$ calculated within the virtual crystal approximation (left) and for the ordered supercell with the homodumbbells Fe–Fe and Co–Co (right). Note that the DOS is for different spin channels here, whereas the values quoted in the text are for the total DOS at the Fermi level, $N(E_F) = N(E_F)^{\text{spin-up}} + N(E_F)^{\text{spin-down}}$.

$Pmn2_1$, $a = 6.4654$ Å, $b = c = 6.2436$ Å). Spin-polarized states were calculated for these two models.

We considered both ferromagnetic and antiferromagnetic spin configurations. However, only the ferromagnetic configuration could be stabilized. A variety of antiferromagnetic spin patterns constructed within the unit cell of $Fe_{1-x}Co_xGa_3$ and within doubled unit cells all converged to a nonmagnetic solution lying higher in energy than the ferromagnetic solution. Therefore DFT calculations on the LDA level put forward the ferromagnetic behavior of $Fe_{1-x}Co_xGa_3$. The variation of the total magnetic moment M with x, as obtained within the virtual crystal approximation, is illustrated in Fig. 2. It shows that the maximal magnetic moment is achieved for $x = 0.5$. A similar result was obtained by Singh [21] for the same number of injected electrons upon the substitution of Ge for Ga in $FeGa_{3-y}Ge_y$. Indeed, on the VCA level, the electronic structure of doped $FeGa_3$ evolves in a nearly rigid-band manner. Therefore no difference between the Fe/Co and Ga/Ge doping should be expected.

The results of our calculations suggest that the half-metallic ferromagnetic state (Fig. 3, left) develops for $0 < x \leqslant 0.5$. It turns to a metallic ferromagnetic state at $0.5 < x < 0.75$ and eventually becomes nonmagnetic at $0.75 \leqslant x \leqslant 1$. This scenario is rather insensitive to the local order. The ordered supercells at $x = 0.5$ also yield a ferromagnetic state with the local moment of 0.48 μ_B for the heteronuclear (Fe–Co) dumbbells and 0.41 μ_B for the homonuclear (Fe–Fe, Co–Co) dumbbells (Fig. 3, right). $Fe_{0.5}Co_{0.5}Ga_3$ has the density of states (DOS) 0.59, 1.53, and 0.65 st./(eV f.u.) at the Fermi energy for the sum of spin directions for the calculation within the VCA, homodumbbells and heterodumbbells approach, respectively. For comparison, for pure $CoGa_3$, we found that the value of DOS at the Fermi energy is 0.93 st./(eV f.u.). Using this DOS value at the Fermi level $N(E_F)$, we calculated the value of the Sommerfeld coefficient $\gamma = (1/3)\pi^2 N(E_F)k_B^2 = 2.19$ mJ/(mol K^2) for $CoGa_3$, which is in a good agreement with the experimental value of 2.6 mJ/(mol K^2) obtained in Ref. [14] from the specific heat data.

The ferromagnetic ground state is indeed observed in $FeGa_{3-y}Ge_y$. The experimental ordered moment of 0.27 μ_B/f.u. at $y = 0.41$ is somewhat lower than the calculated one ($\mu_{\text{LDA}} \sim 0.4$ μ_B/f.u. at $y = 0.4$), as typical for itinerant magnets, where spin fluctuations, which are missing in LDA, lead to a substantial reduction in the ordered moment. In the case of $Fe_{1-x}Co_xGa_3$, the lack of magnetic ordering prevents us from a direct comparison of μ_{LDA} to the experiment. Moreover, we found a qualitative difference between the ferromagnetic behavior, as predicted by LDA, and the antiferromagnetic behavior in $Fe_{0.5}Co_{0.5}Ga_3$, which is evidenced by the negative θ_{CW} observed in $Fe_{1-x}Co_xGa_3$ for $0.1 < x < 0.72$ [15] and additionally supported by the spin-lattice relaxation presented below.

B. NMR in $Fe_{1-x}Co_xGa_3$

There are three NMR active and naturally abundant isotopes in $Fe_{1-x}Co_xGa_3$ compounds suitable for NMR investigation: ^{69}Ga, ^{71}Ga, and ^{59}Co. Our previous ^{69,71}Ga NQR investigations [9] revealed high values of the quadrupole frequencies for both Ga positions in the $Fe_{1-x}Co_xGa_3$ solid solution series. Two inequivalent positions of Ga lead to very broad ^{69,71}Ga NMR spectra with overlapping singularities of the powder pattern. Thus, for the parent semiconductor compound $FeGa_3$ exhibiting the strongest quadrupole splitting, we have measured only the central transition line of the field-sweep NMR spectrum of the ^{71}Ga isotope, which has a lower quadrupole frequency (Fig. 4). This spectrum is a textbook example of the NMR central transition powder pattern in the presence of quadrupole interactions in the second order of perturbation theory. It consists of two contributions: the characteristic double horn line with a step in the middle originating from the Ga1 position with a low asymmetry parameter $\eta = 0.1$ (green line) and the single peak with typical shoulders at the edges, which stems

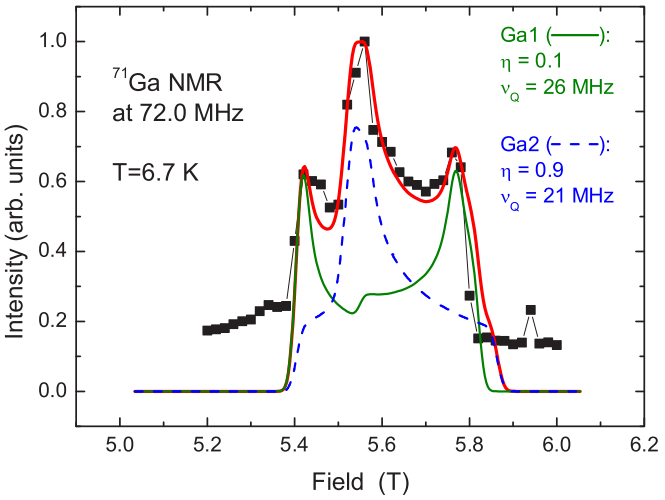

FIG. 4. (Color online) $FeGa_3$: field-sweep NMR spectrum of the central $(-\frac{1}{2} \leftrightarrow +\frac{1}{2})$ transition of the ^{71}Ga nuclei measured at $T = 6.7$ K at 72.0 MHz. Thin lines (blue dashed and green solid) are the numerical simulation for the Ga1 site ($\eta = 0.1$, $\nu_Q = 26.0$ MHz) and Ga2 site ($\eta = 0.9$, $\nu_Q = 21.8$ MHz). The thick red line is the resulting simulation spectrum.

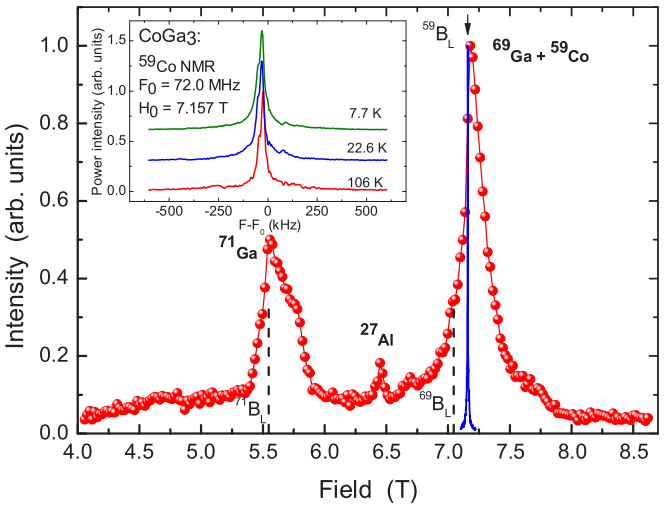

FIG. 5. (Color online) Field-sweep NMR spectrum of $Fe_{0.75}Co_{0.25}Ga_3$ measured at 72.0 MHz at 19 K (red spheres). Vertical dashed lines indicate the position of the Larmor fields for ^{71}Ga and ^{69}Ga. The arrow shows the position of the Larmor field for ^{59}Co. Blue solid line shows ^{59}Co one pulse FT NMR spectrum measured at 22.6 K at $H = 7.157$ T in $CoGa_3$ recalculated to the field domain. Also the position of the ghost ^{27}Al line is shown. (Inset) ^{59}Co one pulse NMR FFT spectra measured at a fixed magnetic field of 7.157 T and a reference frequency of 72.0 MHz.

from the Ga2 site with the high asymmetry parameter $\eta = 0.9$ (blue dashed line). One can see that the observed ^{71}Ga NMR spectrum coincides very well with our NQR results reported in Ref. [9].

With the Co substitution for Fe in $Fe_{1-x}Co_xGa_3$, the ^{71}Ga NMR central transition line broadens and loses its sharp singularities, reflecting the increasing inhomogeneity of the electric field gradient (EFG) distribution, in perfect agreement with the broadening of Ga NQR lines. This is demonstrated in Fig. 5, where the field-sweep spectrum of $Fe_{0.75}Co_{0.25}Ga_3$ is shown. Interestingly, a strong line appears in the field range of 7.0–7.5 T. This line can be assigned to a ^{59}Co NMR signal with some broad background from the ^{69}Ga isotope.

For the opposite side binary compound $CoGa_3$, the NMR spectrum is completely dominated by an extremely narrow ^{59}Co line observed very close to the Larmor field position of the ^{59}Co nuclei at 72.0 MHz (inset of Fig. 5). To measure such a narrow line properly, we had to reduce our spin-echo pulse sequence to one pulse and use the fast Fourier transform (FFT) technique at a fixed magnetic field of 7.157 T. The FFT ^{59}Co spectra measured for $CoGa_3$ at various temperatures are presented in the inset of Fig. 5. The striking narrowness of the ^{59}Co NMR line shows that the Co atom is in a completely nonmagnetic state, donating all nine valence electrons to the conduction band, which results in good metallic properties of $CoGa_3$ [14].

The central transition line of the ^{59}Co NMR spectra in $CoGa_3$ exhibit relatively low second-order quadrupole splitting of about 50 kHz. The reason for this effect might be an effective dynamic screening of the lattice contribution to the electric field gradient (EFG) by conduction electrons, while the on-site contribution to the EFG is almost zero due to an absence of electrons localized on the valence 3*d* and 4*s* shells.

C. Nuclear spin-lattice relaxation (NSLR)

The nuclear spin-lattice relaxation rate (NSLR) $1/T_1$ was measured using the ^{69}Ga nuclei for the Ga1 NQR line (see the bottom inset in Fig. 6) in a wide temperature range of 3–300 K for three $Fe_{1-x}Co_xGa_3$ samples with the Co concentrations $x = 0$, 0.5, and 1.0. For the edge binary compounds, the magnetization recovery curves were single exponential, while for $Fe_{0.5}Co_{0.5}Ga_3$ the stretched exponent function provides better fitting results. The temperature dependence of $^{69}(1/T_1)$

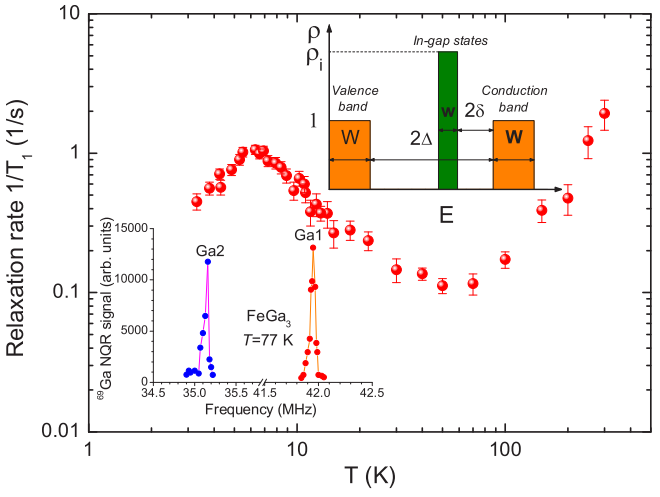

FIG. 6. (Color online) Temperature dependence of the ^{69}Ga NSLR at the Ga1 site in $FeGa_3$. (Bottom inset) The ^{69}Ga NQR spectrum in $FeGa_3$ measured at 77 K. (Top inset) Modified "narrow band-small energy gap" model at $T = 0$ (see text).

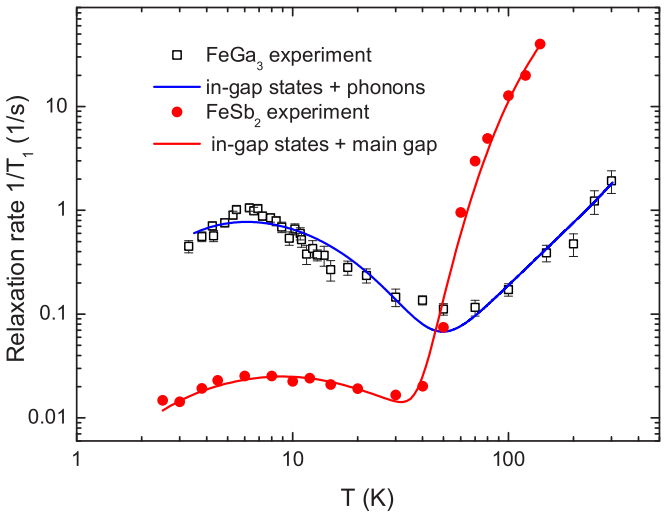

FIG. 7. (Color online) Comparison of the ^{69}Ga spin-lattice relaxation rate in $FeGa_3$ (open squares) and the ^{123}Sb relaxation rate in $FeSb_2$ (closed circles, adopted from Ref. [5]). Solid lines are best fits using the model described in the text.

in $FeGa_3$ is presented in Fig. 6. Surprisingly, it demonstrates a huge unexpected maximum at $T \approx 6$ K with almost a one order of magnitude difference between the $1/T_1$ values at 6 and at 50 K. As will be shown below, this maximum indicates the existence of the in-gap states just below the conduction band. A very similar behavior was observed earlier for the ^{123}Sb NSLR in $FeSb_2$ [5]. The comparison of these NSLR data for $FeGa_3$ and $FeSb_2$ is presented in Fig. 7.

For a quantitative description of our $^{69}(1/T_1)$ data in $FeGa_3$, we used the modified "narrow band–small energy gap" model [22]. It contains two rectangular bands of width W separated by a main gap of 2Δ with a narrow peak of in-gap states of width w with a density of states $\rho_i(\varepsilon) \sim \rho_0 \exp(-T/T_0)$ separated by a small gap of 2δ from the bottom of the conduction band (see Fig. 6, top inset). There are two main temperature regimes in this model. In the low-temperature (LT) regime, the NSLR mechanism is caused by the activation of the localized in-gap electrons over a small gap 2δ into the empty conduction band. This leads to the gradual increase of Ga $1/T_1(T)$ with increasing temperature from the lowest $T \sim 3$ K to the temperature of the NSLR maximum around 6 K. The narrow in-gap peak $\rho_i(\varepsilon)$ disappears at higher temperatures due to its broadening and overlap with the conduction band, resulting in the decreasing NSLR and in the appearance of a clearly pronounced minimum on $1/T_1(T)$ at 50–60 K. Then, in the high-temperature (HT) regime, $1/T_1$ starts increasing again due to the electron activation across the main energy gap 2Δ.

In general, the NSLR can be expressed as

$$\frac{1}{T_1} = \frac{\hbar k_B T}{\omega} \sum_q A^2 F(q) \chi''_{q,w}, \tag{1}$$

where $\chi''_{q,w} \approx \frac{\pi}{k_B T} \int d\varepsilon f(\varepsilon)[1 - f(\varepsilon)]\rho^2(\varepsilon)$ is the imaginary part of the dynamical susceptibility; $f(\varepsilon) = [\exp(\varepsilon/T) + 1]^{-1}$ is the Fermi distribution function, A is the hyperfine interaction constant, $F(q)$ is the form-factor depending on the geometry. Assuming a weak q and ω dependence of A and $F(q)$ and using the equation $-T\delta f/\delta\varepsilon = f(\varepsilon)[1 - f(\varepsilon)]$, one obtains after integration of Eq. (1) over the rectangular bands:

$$\frac{1}{T_1} \propto T\left\{\rho_d^2[f(\Delta) - f(\Delta + W)] + \rho_i^2[f(\delta) - f(\delta + \omega)]\right\}. \tag{2}$$

Here, the first term is responsible for the activationlike relaxation behavior in the HT regime, while the second one causes the pronounced maximum in the LT regime. To complete the relaxation scenario, one should add to Eq. (2) the phonon-induced quadrupole relaxation involving two-phonon (Raman) scattering, which is active already at moderate temperatures. Indeed, the EFG at the Ga site is strongly affected by thermal fluctuations. The interaction of the fluctuating EFG with the quadrupole moments of the Ga nuclei causes the quadrupole relaxation, for which the relaxation rate increases with temperature as T^2 (see Refs. [23,24]):

$$\frac{1}{T_1} \propto \frac{9k_B^2}{8\pi^3\hbar^3} \frac{e^2\gamma Q}{R^3} T^2, \tag{3}$$

where γ is the gyromagnetic ratio, Q the quadrupole moment, and R the interatomic distance. Adding Eq. (3) in a more general power form $1/T_1 = AT^n$ to the expression (2), one arrives for $FeGa_3$ at

$$\frac{1}{T_1} \propto T\left\{\rho_d^2[f(\Delta) - f(\Delta + W)] + \rho_i^2[f(\delta) - f(\delta + \omega)]\right\} + AT^n. \tag{4}$$

Using Eq. (4), we succeeded to fit the experimental ^{69}Ga $1/T_1$ data in the entire investigated temperature range 3–300 K. The best fit of the experimental $1/T_1$ data to Eq. (4) (blue solid line in Fig. 7) gives the power factor $n \approx 2$ confirming the T^2 behavior characteristic for the phonon relaxation mechanism driven by the two-phonon (Raman) scattering.

For comparison, we used Eq. (4) to fit the experimental ^{123}Sb $1/T_1(T)$ data for $FeSb_2$ between $T = 2.5$–150 K adapted from Ref. [5]. The best fitting curve for $FeSb_2$ is shown in Fig. 7 by the red solid line. The resulting fitting parameters for $FeSb_2$ and $FeGa_3$ are presented in Table I. As seen from these values, the in-gap states in both compounds indeed form a very narrow layer with a width of $w = 1$ K (26 K) separated from the bottom of the conduction band only by $2\delta = 13$ K (8 K) for $FeGa_3$ ($FeSb_2$).

It is worth comparing the relative capacity of the in-gap state level in $FeGa_3$ and $FeSb_2$ estimated as $n_0 = (\rho_0 w)/(\rho_W W)$, where $\rho_W = 1$ is the normalized height of the main rectangular bands. As seen from Table I, this value is about 16 times higher in $FeGa_3$ than in $FeSb_2$. This explains the much stronger and more pronounced $1/T_1(T)$ maximum at low temperatures observed in $FeGa_3$ in comparison to that in $FeSb_2$ (Fig. 7). The obtained main gap $E_g = 2\Delta$ value in $FeGa_3$ is in perfect agreement with our *ab initio* calculations $2\Delta_{ab initio} \approx 0.4$ eV (≈4700 K) [9]. From this result, one can expect different scenarios for $1/T_1(T)$ in the HT regime for $FeGa_3$ and $FeSb_2$. Actually, the energy gap value of 2Δ for $FeGa_3$ is nearly seven times larger than that for $FeSb_2$: 5500 K versus 800 K, respectively. This means that in the investigated HT regime

TABLE I. Best fit parameters according to the modified "narrow band-small energy gap" model [22] (see text and upper inset of Fig. 6). Accuracy of the in-gap states fitting parameters $(\omega, \delta, \rho_0, T_0)$ is about 10–20%.

Parameter	$FeGa_3$	$FeSb_2$
In-gap layer separation from the conduction band, 2δ	13 K	8 K
Main gap, 2Δ	5500 K	800 K
In-gap layer width, w	1 K	26 K
Main band width, W	75 K	1100 K
Zero T height of the in-gap layer, normalized to the main rectangle Band height, ρ_0	1.73 K^{-1}	0.06 K^{-1}
Characteristic temperature scale for in-gap state density of states T_0	11.5 K	10.6 K
Relative zero T capacity of the in-gap layer, $n_0 = (\rho_0 w)/(\rho_W W)$	2.3×10^{-2}	1.4×10^{-3}

40–300 K the thermal activation of electrons across the main gap is rather inefficient for $FeGa_3$ yet.

Summarizing the above consideration, the spin-lattice relaxation in $FeGa_3$ and $FeSb_2$ can be decomposed into three parts:

$$\left(\frac{1}{T_1}\right)_{\Sigma} = \left(\frac{1}{T_1}\right)_{\text{in-gap}} + \left(\frac{1}{T_1}\right)_{\text{act}} + \left(\frac{1}{T_1}\right)_{\text{ph}}, \qquad (5)$$

where $(T_1^{-1})_{\text{in-gap}}$ is the magnetic relaxation caused by activation from the in-gap states into conduction band; $(T_1^{-1})_{\text{act}}$ is the magnetic relaxation due to activation of electrons over the main energy gap $E_g = 2\Delta$, and $(T_1^{-1})_{\text{ph}}$ is the quadrupole relaxation caused by phonons.

The interplay between these components determines the observed temperature behavior of the spin-lattice relaxation in $FeGa_3$ and $FeSb_2$. At low temperatures ($T < 40$ K), the first term of Eq. (5) gives the main contribution to $1/T_1$ in both $FeGa_3$ and $FeSb_2$ providing a pronounced maximum of $1/T_1(T)$ at $T_{\max} \approx 6$ and 10 K, respectively. With increasing temperature, other terms in Eq. (5) start to dominate causing the fast increase in $1/T_1$. In $FeSb_2$, the energy gap E_g is relatively small and the main relaxation channel is the activation with an exponential growth of $1/T_1$. In contrast, $FeGa_3$ exhibits a much larger gap value making the activation process ineffective, which results in a dominance of the phonon relaxation in the temperature range 40–300 K.

This relaxation scenario in $FeGa_3$ is independently confirmed by the isotope effect analysis. In the case of a pure magnetic relaxation mechanism, the ratio of the relaxation rates $^{69}(1/T_1)/^{71}(1/T_1)$ of the ^{69}Ga and ^{71}Ga isotopes should be equal to $(^{69}\gamma/^{71}\gamma)^2 = 0.62$, where γ is the gyromagnetic ratio of the corresponding nuclei, while in the opposite case of a pure quadrupole relaxation mechanism $^{69}(1/T_1)/^{71}(1/T_1) = (^{69}Q/^{71}Q)^2 = 2.51$, where Q is the quadrupole moment of the nuclei. The experimental $^{69}(1/T_1)/^{71}(1/T_1)$ data as a function of temperature are shown in Fig. 8. As clearly seen from this figure, in the low-temperature range from 2 to 40 K the relaxation mechanism is exclusively magnetic, which implies that the in-gap states in $FeGa_3$ manifest pronounced magnetic behavior. With further increase in temperature, the quadrupolar contribution to the total relaxation rate increases rapidly. Finally, above 100 K, one arrives at the mixed case of both magnetic and quadrupole channels of nuclear relaxation with the pronounced domination of the latter. This result is in good agreement with the analysis described above.

The in-gap states seem to be responsible for the giant thermopower observed at the verge of magnetism if Fe based semimetals $FeSb_2$ [7,25], $Fe_{1-x}M_xSi$ alloys (M = Co, Ir, Os) [26] and $FeGa_3$ [9,11]. Just recently, in-gap states earned an increased attention because the question arises if these metallic and magnetic states are located at the surface and therefore have a topological origin. SmB_6 can be considered as a prototype of a topological semimetal [27].

Owing to its good metallic properties, the opposite edge binary compound $CoGa_3$ exhibits a Korringa-like linear ^{69}Ga spin-lattice relaxation (Fig. 9) caused by the contact interaction between the conduction electrons and ^{69}Ga nuclei:

$$\left(\frac{1}{T_1}\right)_K = \pi\hbar^3\gamma_e^2\gamma_n^2 A_{\text{hf}}^2 N^2(E_F) k_B T = a_K T, \qquad (6)$$

where γ_e and γ_n are the gyromagnetic ratios for electron and nucleus, respectively, A_{hf} is the contact hyperfine coupling between conduction electrons and nuclei, $N(E_F)$ is the density of states at the Fermi level, and a_K is the Korringa coefficient. As seen from Fig. 9, the experimental $^{69}[1/T_1(T)]$ data for $CoGa_3$ can be perfectly approximated by Eq. (6) in the entire investigated temperature range of 12–300 K with the best fit value of $a_K = 0.15$ (here and further T is in K and T_1 is in seconds). Using the experimental Korringa constant value $a_K = 1/T_1T = 0.15K^{-1}s^{-1}$ for $CoGa_3$ and Eq. (6), we estimated the hyperfine constant on the Ga as $A_{hf}(^{69}\text{Ga}) = 7.7T/\mu_B$.

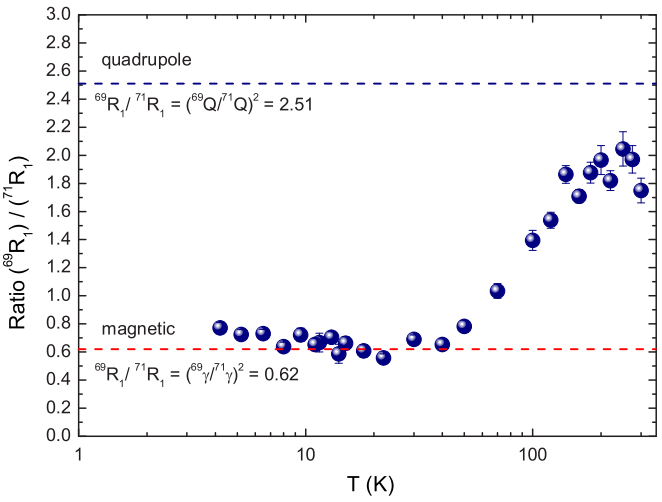

FIG. 8. (Color online) Ratio of the spin-lattice relaxation rates for ^{69}Ga and ^{71}Ga as a function of temperature in $FeGa_3$. Dashed lines indicate the values for pure quadrupolar and pure magnetic relaxation mechanism.

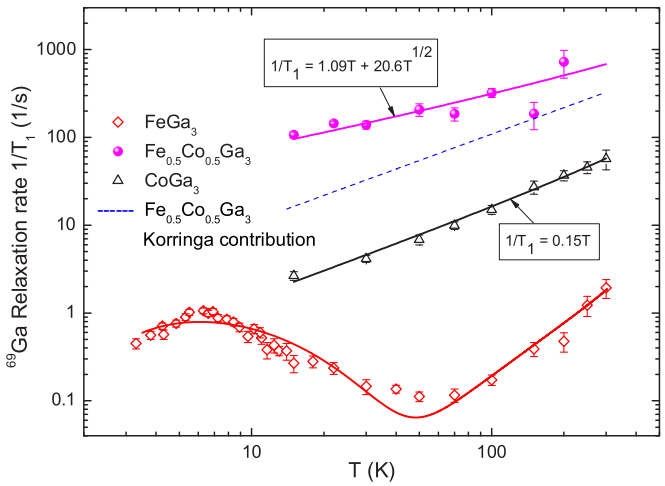

FIG. 9. (Color online) Temperature dependence of the spin-lattice relaxation rate $1/T_1$ for $FeGa_3$, $CoGa_3$, and $Fe_{0.5}Co_{0.5}Ga_3$. Solid lines are best fits using the models described in the text.

A very fast relaxation rate is shown by the $Fe_{0.5}Co_{0.5}Ga_3$ compound: more than one order of magnitude faster than in $CoGa_3$ (Fig. 9). At a first glance, it is quite natural since according to our band-structure calculations [9] the ratio of the squared densities of states at the Fermi level for $Fe_{0.5}Co_{0.5}Ga_3$ and $CoGa_3$ $N^2_{E_F}(Fe_{0.5}Co_{0.5}Ga_3)/N^2_{E_F}(CoGa_3) = 7.26$. Therefore the linear Korringa coefficient for $Fe_{0.5}Co_{0.5}Ga_3$ can be estimated as

$$a_K(Fe_{0.5}Co_{0.5}Ga_3) = 7.26 \times a_K(CoGa_3) = 1.09. \quad (7)$$

The linear Korringa function $1/T_1 = 1.09 \times T$ is plotted in Fig. 9 by the dashed line. It is indeed above the relaxation data for $CoGa_3$ but still far below the experimental $1/T_1$ data for the $Fe_{0.5}Co_{0.5}Ga_3$ compound. Moreover, it has a wrong decline in the double logarithmic scale of Fig. 9. This result unambiguously shows that the spin-lattice relaxation in $Fe_{0.5}Co_{0.5}Ga_3$ is dominated by a mechanism other than the Korringa mechanism. The model that describes our relaxation data in $Fe_{0.5}Co_{0.5}Ga_3$ is the Moriya's spin-fluctuation theory [28]. According to this theory for weak (low T_N) or nearly antiferromagnetic (AF) metals, the nuclear spin-lattice relaxation is given by the equation

$$\frac{1}{T_1} = \frac{\alpha T}{(T - T_N)^{1/2}}. \quad (8)$$

For $T \gg T_N \approx 0$, Eq. (8) is reduced to a square root temperature dependence $1/T_1 \propto T^{1/2}$, which is a unique feature of weakly and nearly AF metals [28]. As shown in Fig. 9, our experimental $1/T_1$ data for $Fe_{0.5}Co_{0.5}Ga_3$ can be successfully fitted by a combination of the linear Korringa term and spin-fluctuation contribution with dominance of the latter:

$$\frac{1}{T_1} = 1.09 \times T + 20.6 \times T^{1/2}. \quad (9)$$

This result is very similar to that observed by ^{55}Mn NMR in β-Mn, which is an AF metal subjected to a strong magnetic frustration ($T_N \approx 0$) [29]. The ^{55}Mn relaxation in β-Mn is mainly due to spin fluctuations, with a minor contribution from contact Korringa interactions: $1/T_1 = 1.7 \times T + 35.3 \times T^{1/2}$ (same units for T and T_1). Pure spin-fluctuation scenario of nuclear spin-lattice relaxation with $1/T_1 \propto T^{1/2}$ in the wide temperature range of 2–300 K was observed by ^{139}La NMR in filled skutterudites $La_{0.9}Fe_4Sb_{12}$ [30].

IV. SUMMARY AND CONCLUSIONS

Our experimental and computational study puts forward the complex magnetic behavior of the $Fe_{1-x}Co_xGa_3$ solid solution. According to the NSLR data, the median compound $Fe_{0.5}Co_{0.5}Ga_3$ reveals strong spin fluctuations that are characteristic of a weakly antiferromagnetic metal. This observation is consistent with the negative (antiferromagnetic) θ_{CW} obtained in the Curie-Weiss fit of the magnetic susceptibility reported in literature [14–16]. However, the Curie-Weiss behavior at high temperatures is generic for itinerant ferromagnets only [31]. Itinerant antiferromagnets will typically show a weak temperature dependence of χ above T_N [31]. Although itinerant electrons may accidentally mimic the Curie-Weiss-type behavior at high temperatures, it is more plausible to assume that the $Fe_{1-x}Co_xGa_3$ solid solution combines features of the itinerant and localized antiferromagnets.

In fact, both itinerant and localized magnetism can be envisaged for this system. Metallic conductivity of the $Fe_{1-x}Co_xGa_3$ solid solutions with $x \geqslant 0.075$ implies the sizable concentration of itinerant electrons. On the other hand, the Fe/Co disorder on the transition-metal site may lead to at least partial localization, because the Fe and Co $3d$ states provide dominant contribution at the Fermi level [9,21]. The latter mechanism is not operative in $FeGa_{3-y}Ge_y$, where the disorder is introduced on the Ga site. Indeed, the Ge containing solid solutions are ferromagnetic [15], as predicted by LDA. They do not show any signatures of the localized magnetism. Their Curie-Weiss behavior at high temperatures can be well ascribed to the itinerant ferromagnetism. The ratio of the effective and ordered moments in the Rhodes-Wohlfarth plot follows the trend typical for itinerant ferromagnets (see Fig. 6 in Ref. [15]).

Remarkably, the apparent antiferromagneticlike behavior of $Fe_{1-x}Co_xGa_3$ is not matched by the LDA results that predict the ferromagnetic nature of electron-doped $FeGa_3$ irrespective of the doping mechanism. While band-structure calculations do not fully account for the Fe/Co disorder, our results for the ordered supercells suggest that the ferromagnetic nature of $Fe_{1-x}Co_xGa_3$ is quite robust within LDA and only weakly depends on the local order of the Fe and Co atoms. Therefore the discrepancy between LDA and the experiment can not be ascribed to a simple mixing of the Fe and Co atoms forming the Fe–Fe, Fe–Co, and Co–Co dumbbells. It rather pertains to a more complex interplay of the itinerant and localized electrons that arise from this mixing. This conjecture is in line with the computational results by Singh [21], who was able to stabilize an antiferromagnetic solution in pure $FeGa_3$, but only by adding the on-site Coulomb repulsion U that creates local moments on Fe.

We have shown that in the parent compound $FeGa_3$, the ^{69,71}Ga spin-lattice relaxation rate $1/T_1(T)$ reveals an unexpected huge maximum at low temperatures with an essentially magnetic relaxation mechanism indicating the

presence of an enhanced density of in-gap states placed near the Fermi energy. These states frequently are assigned being responsible for the giant thermopower in Fe based semimetals at low temperatures [7,11,25,26]. Only above ~70 K, when the in-gap level is completely empty, the nuclear spin-lattice relaxation exhibits a crossover to a phonon mechanism characteristic of quadrupolar nuclei in nonmagnetic systems. The other end member, $CoGa_3$, is a band metal. It demonstrates the metallic Korringa behavior of the spin-lattice relaxation with $1/T_1 \propto T$. The mixing of these well-understood $FeGa_3$ and $CoGa_3$ compounds triggers strong and unexpected antiferromagnetic spin fluctuations. Indeed, in the intermediate $Fe_{0.5}Co_{0.5}Ga_3$ compound, $1/T_1(T)$ is strongly (by nearly two orders of magnitude) enhanced due to spin fluctuations, with $1/T_1 \propto T^{1/2}$ in perfect agreement with Moriya's spin-fluctuation theory for itinerant magnetic systems. Such a $1/T_1(T)$ behavior is a unique feature of weakly and nearly AF metals. The $Fe_{1-x}Co_xGa_3$ compounds with x close to 0.5 seem to be very close to magnetic ordering, which is prohibited probably by strong spin fluctuations and the structural disorder between the different T–T dumbbells, in contrast to the $FeGa_{3-y}Ge_y$ system, which has a regular arrangement of solely homoatomic Fe–Fe dumbbells and exhibits a FM order at certain doping values.

ACKNOWLEDGMENTS

This work was supported in part by the MSU priority program; Russian Foundation for Basic Research, Grants Nos. 11-08-00868-a, 14-03-31181 mol_a; joint Russian-Taiwan Grant RFBR-NSC No. 12-03-92002-NSC_a (101-2923-M-006-001-MY2). A.A.G., N.B., and W.K. acknowledge financial support by the Deutsche Forschungsgemeinschaft (DFG) via TRR 80 (Augsburg-Munich). M.S. acknowledges the US National Science Foundation for the support of research on itinerant magnetism in intermetallic compounds via the NSF-CAREER Grant DMR-0955353. The work in Tallinn has been supported by the Mobilitas program of the ESF (Grant MTT77). A.A.T. acknowledges insightful discussions with Christoph Geibel and Deepa Kasinathan. S.M. Kazakov is acknowledged for his help with XRD experiments.

[1] U. Häussermann, M. Boström, P. Viklund, Ö. Rapp, and T. Björnängen, J. Solid State Chem. **165**, 94 (2002).
[2] V. Jacarino, G. K. Wertheim, J. H. Wernick, L. R. Walker, and S. Arajs, Phys. Rev. **160**, 476 (1967).
[3] D. Mandrus, J. L. Sarrao, A. Migliori, J. D. Thompson, and Z. Fisk, Phys. Rev. B **51**, 4763 (1995).
[4] C. Petrovic, J. W. Kim, S. L. Bud'ko, A. I. Goldman, P. C. Canfield, W. Choe, and G. J. Miller, Phys. Rev. B **67**, 155205 (2003).
[5] A. A. Gippius, K. S. Okhotnikov, M. Baenitz, and A. V. Shevelkov, Solid State Phenom. **152-153**, 287 (2009).
[6] B. C. Sales, E. C. Jones, B. C. Chakoumakos, J. A. Fernandez-Baca, H. E. Harmon, J. W. Sharp, and E. H. Volckmann, Phys. Rev. B **50**, 8207 (1994).
[7] A. Bentien, S. Johnsen, G. K. H. Madsen, B. B. Iversen, and F. Steglich, Europhys. Lett. **80**, 17008 (2007).
[8] Z. P. Yin and W. E. Pickett, Phys. Rev. B **82**, 155202 (2010).
[9] V. Yu. Verchenko, M. S. Likhanov, M. A. Kirsanova, A. A. Gippius, A. V. Tkachev, N. E. Gervits, A. V. Galeeva, N. Büttgen, W. Krätschmer, C. S. Lue, K. S. Okhotnikov, and A. V. Shevelkov, J. Solid State Chem. **194**, 361 (2012).
[10] N. Tsujii, H. Yamaoka, M. Matsunami, R. Eguchi, Y. Ishida, Y. Senba, H. Ohashi, S. Shin, T. Furubayashi, H. Abe, and H. Kitazawa, J. Phys. Soc. Jpn. **77**, 024705 (2008).
[11] C. S. Lue, W. J. Lai, and Y. K. Kuo, J. Alloys Compd. **392**, 72 (2005).
[12] Z. Fisk, J. L. Sarrao, J. D. Thompson, D. Mandrus, M. F. Hundley, A. Miglori, B. Bucher, Z. Schlesinger, G. Aeppli, E. Bucher, J. F. DiTusa, C. S. Oglesby, H-R. Ott, P. C. Canfield, and S. E. Brown, Physica B **206-207**, 798 (1995).
[13] G. Aeppli and Z. Fisk, Comm. Condens. Matter Phys. **16**, 155 (1992).
[14] E. E. Bittar, C. Capan, G. Seyfarth, P. Pagliuso, and Z. Fisk, J. Phys.: Conf. Ser. **200**, 012014 (2010).
[15] K. Umeo, Y. Hadano, S. Narazu, T. Onimaru, M. A. Avila, and T. Takabatake, Phys. Rev. B **86**, 144421 (2012).
[16] Y. Hadano, S. Narazu, M. Avila, T. Onimaru, and T. Takabatake, J. Phys. Soc. Jpn. **78**, 013702 (2009).
[17] D. Bogdanov, K. Winzer, I. Nekrasov, and T. Pruschke, J. Phys.: Condens. Matter. **19**, 232202 (2007).
[18] K. Koepernik and H. Eschrig, Phys. Rev. B **59**, 1743 (1999).
[19] J. P. Perdew and Y. Wang, Phys. Rev. B **45**, 13244 (1992).
[20] P. E. Blöchl, O. Jepsen, and O. K. Andersen, Phys. Rev. B **49**, 16223 (1994).
[21] D. J. Singh, Phys. Rev. B **88**, 064422 (2013).
[22] T. Caldwell, A. P. Reyes, W. G. Moulton, P. L. Kuhns, M. J. R. Hoch, P. Schlottmann, and Z. Fisk, Phys. Rev. B **75**, 075106 (2007).
[23] R. Mieher, Phys. Rev. **125**, 1537 (1962).
[24] J. van Kranendonk, Physica **20**, 781 (1954).
[25] V. G. Storchak, J. H. Brewer, R. L. Lichti, R. Hu, and C. Petrovic, J. Phys.: Condens. Matter **24**, 185601 (2012).
[26] B. C. Sales, O. Delaire, M. A. McGuire, and A. F. May, Phys. Rev. B **83**, 125209 (2011).
[27] M. Dzero, K. Sun, P. Coleman, and V. Galitski, Phys. Rev. B **85**, 045130 (2012).
[28] T. Moriya, in *Spin Fluctuation in Itinerant Electron Magnetism* (Springer-Verlag, Berlin, 1985).
[29] M. Katayama, J. Phys. Soc. Jpn. **42**, 97 (1977).
[30] A. A. Gippius, M. Baenitz, E. Morozova, A. Leithe-Jasper, W. Schnelle, A. Shevelkov, E. Alkaev, A. Rabis, J. Mydosh, Yu. Grin, and F. Steglich, J. Magn. Magn. Mater. **300**, e403 (2006).
[31] T. Moriya, J. Magn. Magn. Mater. **14**, 1 (1979).